




## Article

# Effective removal of hexavalent chromium with magnetically reduced graphene oxide bentonite

Shoufa Cao<sup>1</sup>, Jingmao Guo<sup>1</sup>, Jianchao Ma<sup>1\*</sup> , Enqing Chen<sup>2</sup>, Jin Pang<sup>1</sup>, Siyu Zhang<sup>1</sup>, Haidong Hao<sup>1</sup>, Danlei Wu<sup>1</sup> and Shaobin Wang<sup>3</sup>

<sup>1</sup>College of Mining Engineering, Taiyuan University of Technology, Taiyuan 030024, Shanxi, P.R. China; <sup>2</sup>Department of Architecture, Lüliang University, Lüliang, 033001, Shanxi, P.R. China and <sup>3</sup>School of Chemical Engineering and Advanced Materials, The University of Adelaide, Adelaide, South Australia 5005, Australia

### Abstract

Water pollution by hexavalent chromium (Cr(VI)) is widespread and problematic. As a result, more research into economic Cr(VI) removal is needed. In this study, we created and employed an adsorption–reduction mechanism to remove Cr(VI). Magnetically reduced graphene oxide bentonite (MrGO-BT) is acid resistant and can undergo magnetic separation. The hydroxyl group of chitosan (CS) condensed with the functional groups on the surface of bentonite (BT), and the MrGO-BT sandwich has been fabricated and constructed from an Fe<sub>3</sub>O<sub>4</sub> core layer sandwiched by reduced graphene oxide (rGO) and a BT shell, with CS acting as a crosslinker. Cr(VI) elimination by MrGO-BT was exothermic and spontaneous according to thermodynamic analyses. The adsorption kinetics and adsorption isotherms were characterized by the pseudo-second order kinetic theory and the Langmuir model, respectively. Regarding the elimination of Cr(VI), the greatest adsorption ability for Cr(VI) elimination achieved was 91.5 mg g<sup>-1</sup>. Fourier-transform infrared spectroscopy and X-ray photoelectron spectroscopy suggested that Cr(VI) was reduced by C–O–H on MrGO-BT to produce Cr(III) and H–C=O, and that Cr(III) chelated with amino groups or exchanged with BT after intercalation. In addition, the introduction of Cu<sup>2+</sup> increased the positive charge of MrGO-BT and amplified the electrostatic interaction between Cr<sub>2</sub>O<sub>7</sub><sup>2-</sup> and HCrO<sub>4</sub><sup>-</sup>, which is what caused Cr(VI) to be eliminated. Cu<sup>2+</sup> and reduced Cr(III) combined with -NH<sub>2</sub> on the surface of MrGO-BT to form -NH–Cr(III) or -NH–Cu<sup>2+</sup>, and Cr(VI) elimination *via* chelation and ion exchange was confirmed. MrGO-BT is shown to be an adsorbent with high acid resistance and good magnetic responsiveness and stability.

**Keywords:** bentonite, Cr(VI) removal, magnetically reduced graphene oxide, reduction of Cr(VI)

(Received 24 August 2022; revised 5 February 2023; Accepted Manuscript online: 16 February 2023; Associate Editor: Chun Hui Zhou)

One of the frequent and problematic contaminants from sectors including mining, electroplating and pharmaceuticals is wastewater that contains hexavalent chromium (Cr(VI); Almeida *et al.*, 2019). Cr(VI) is thought to be extremely poisonous and poorly biodegradable, which poses a major threat to environmental ecology as well as human health (Kumar *et al.*, 2007; Li *et al.*, 2017; Muthumareeswaran *et al.*, 2017; Maitlo *et al.*, 2019). As a result, effluents containing Cr(VI) must be treated or transformed into less hazardous Cr(III) using various methods. Among these, adsorption represents a promising strategy due to its simplicity and efficiency and the wide variety of available adsorbents. It has been demonstrated that many adsorbents, including carbon, chitosan (CS) and biochar, have excellent Cr(VI)-removal capabilities (Tran *et al.*, 2019). However, their activity is limited by acidic conditions or the existence of coexisting cations (e.g. Cu<sup>2+</sup>; Chen *et al.*, 2020). Therefore, a high-efficiency, acid-resistant Cr(VI) adsorbent is needed for when coexisting cations are present.

Reduced graphene oxide (rGO) can remove metal cations effectively because of its negative charge and chemisorption functional groups (Yu *et al.*, 2021). However, rGO could see reduced adsorption performance and commercial applicability in aqueous solutions because of its high price, irreversible aggregation and accumulation and poor adsorption selectivity under acidic conditions (Abu-Nada *et al.*, 2020). Therefore, numerous researchers have tried to functionalize rGO with clay minerals to improve its dispersibility and performance. Montmorillonite (Mnt) has been a focus of researchers because of its wide accessibility and low cost. rGO-Mnt hybrids have great chemical stability and have been shown to remove Cr(VI) efficiently (Peng *et al.*, 2020; Zhao *et al.*, 2020). For example, Zhang *et al.* (2018) synthesized an rGO-Mnt that could remove 94.87% of Cr(VI) from an initial Cr(VI) solution at a concentration of 20 mg L<sup>-1</sup> at 35°C. Nevertheless, the significant dispersion and suspension of rGO-Mnt in the solution resulted in low recyclability. Recently, a combination of magnetic separation and adsorption processes with the addition of Fe<sub>3</sub>O<sub>4</sub> improved the separating efficiency of an adsorbent from wastewater (Shan *et al.*, 2018; Sun *et al.*, 2019). However, protecting Fe<sub>3</sub>O<sub>4</sub> from acid corrosion is key in acidic Cr(VI) wastewaters. Previous research has shown that Fe<sub>3</sub>O<sub>4</sub> coated with CS exhibited good acid corrosion resistance

\*E-mail: majianchao@tyut.edu.cn

**Cite this article:** Cao S, Guo J, Ma J, Chen E, Pang J, Zhang S, Hao H, Wu D, Wang S (2023). Effective removal of hexavalent chromium with magnetically reduced graphene oxide bentonite. *Clay Minerals* 58, 7–18. <https://doi.org/10.1180/clm.2023.4>

(Feng *et al.*, 2019). Furthermore, due to its distinctive sandwich structure, great chemical stability and mechanical stability, bentonite (BT), which has smectite as its primary component, is a common, inexpensive natural clay that is capable of eliminating Cr(VI) from sewage. Loading rGO over magnetically modified smectite may be effective in terms of providing an affordable and highly effective Cr(VI) removal material. A magnetically reduced graphene oxide bentonite (MrGO-BT) material has not been reported previously in the literature.

Here, an MrGO-BT material was developed for the joint adsorption of Cu<sup>2+</sup> and Cr(VI). The removal effectiveness of MrGO-BT for Cr(VI) and the associated adsorption isotherms, kinetics and thermodynamics were investigated. Analyses were conducted regarding the Cr(VI) elimination process. We also investigated and tested the acid resistance and reusability of MrGO-BT and the influence of Cu<sup>2+</sup> on Cr(VI) elimination.

## Experimental

### Materials and reagents

Analytically pure sulfuric acid, sodium hydroxide, hydrogen peroxide, hydrochloric acid, ferric chloride hexahydrate, sodium nitrate, sodium acetate anhydrous, glycol, potassium permanganate, CS, acetic acid, epichlorohydrin, ethylenediaminetetraacetic acid disodium salt, potassium dichromate and cupric chloride dehydrate were obtained from Sinopharm Chemical Reagent Co., Ltd (P.R. China). Natural sodium BT was acquired from Runlong Bentonite Co., Ltd (P.R. China), and its cation-exchange capacity was 88 mmol 100 g<sup>-1</sup>. The chemical constitution (wt.%) of the BT was: SiO<sub>2</sub> = 71.20; TiO<sub>2</sub> = 0.10; Al<sub>2</sub>O<sub>3</sub> = 13.00; Fe<sub>2</sub>O<sub>3</sub> = 0.75; FeO = 0.17; MnO = 0.07; CaO = 1.62; K<sub>2</sub>O = 1.01; Na<sub>2</sub>O = 0.83; and P<sub>2</sub>O<sub>3</sub> = 0.04. Graphene oxide (GO) was fabricated using a modified Hummers method.

### Characterization

X-ray diffraction (XRD) was conducted using a Rigaku Max 2550 VB/PC device (Japan) at a step size of 4°2θ min<sup>-1</sup> over 5–85°2θ. Fourier-transform infrared (FTIR) spectroscopy was recorded at 400–4000 cm<sup>-1</sup> using a Tensor 27 device (Bruker, Germany). Transmission electron microscopy (TEM) images were obtained using a JEM-2100 F device (JEOL, Japan). Energy-dispersive spectroscopy (EDS) was conducted using a X-Max N (Tescan, Czechia). The specific surface area and pore size of the material were measured using an ASAP-2020 C (USA) and calculated using the Brunner–Emmett–Teller (BET) method. The ζ-potential was measured using a JS-94 Zeta microelectrophoresis apparatus (China). The element valence change was determined using X-ray photoelectron spectroscopy (XPS; Amicus, Shimadzu Co., Japan).

### Preparation of MrGO-BT

A flask containing H<sub>2</sub>SO<sub>4</sub> (250 mL) was placed into an ice bath and then NaNO<sub>3</sub> (2.5 g) and natural graphite (5 g) were added and stirred for 15 min. KMnO<sub>4</sub> (32 g) was transferred to the flask and mechanical agitation was conducted for 30 min at 10°C. This was then heated to 35°C and held at that temperature for 60 min. After that, distilled water (240 mL) was added and heated to 98°C. After mechanical agitation for 25 min, more distilled water (1000 mL) was added, and 30% H<sub>2</sub>O<sub>2</sub> was then added

to the mixture until the pH was 7.0. GO was acquired after filtering and vacuum drying at 60°C for 24 h (Marcano *et al.*, 2010).

For the preparation of MrGO, CS (2.4 g), GO (0.1 g), FeCl<sub>3</sub>·6H<sub>2</sub>O (2.0 g) and CH<sub>3</sub>COONa (5.3 g) were added to 40 mL of ethylene glycol and mixed for 40 min. Then, the solution was placed in an autoclave at 200°C for 12 h. After cooling, MrGO was acquired by washing (0.5% (v/v) CH<sub>3</sub>COOH) and drying at 60°C for 12 h.

For the synthesis of MrGO-BT, 100 mL CH<sub>3</sub>COOH (1.5% (v/v)) was added to a flask and then preheated to 30°C for 10 min. After that, MrGO powder (0.5 g) was dispersed in a round-bottomed flask filled with nitrogen, and this was stirred at 30°C for 20 min. Then, natural sodium BT (2 g) and epichlorohydrin (2 mL) were added, and this was then heated to 55°C for 2 h. After cooling, MrGO-BT was obtained after washing and drying at 60°C for 12 h.

### Adsorption experiments

The adsorption of mixed ions of Cu<sup>2+</sup> and Cr(VI) was investigated following the Cr(VI) adsorption studies. NaOH and HCl solutions were used to alter the pH. The water samples were collected after filtration through a 22 μm membrane. The remaining Cr(VI) and Cu<sup>2+</sup> concentrations were chosen following ultraviolet–visible spectroscopy. The adsorption ability at equilibrium ( $q_e$  (mg g<sup>-1</sup>)) was calculated according to Equation 1:

$$q_e = \frac{C_0 - C_e}{m} \times V \quad (1)$$

where  $C_0$  and  $C_e$  are the starting and equilibrium concentrations (mg L<sup>-1</sup>) of Cr(VI) or Cu<sup>2+</sup> in solution, respectively,  $V$  is the solution volume of Cr(VI) or Cu<sup>2+</sup> (L) and  $m$  is the amount of adsorbent added (g).

The elimination rate ( $R$ ) for heavy-metal ion adsorption on MrGO-BT was determined using Equation 2:

$$R (\%) = \frac{(C_0 - C_e)}{C_0} \times 100\% \quad (2)$$

### Adsorption kinetics

Use of pseudo-first order and pseudo-second order kinetic models were used for fitting to the adsorption process. The linear shape of the first-order kinetic model can be expressed as is shown in Equation 3:

$$\ln(q_e - q_t) = \ln q_e - k_1 t \quad (3)$$

where  $q_e$  and  $q_t$  are the adsorption amounts of Cr(VI) (mg g<sup>-1</sup>) at steady state and at any time  $t$  (min), respectively, and  $k_1$  is the velocity constant for first-order adsorption (min<sup>-1</sup>).

The linear form of the second-order kinetic model can be represented as is shown in Equation 4:

$$\frac{t}{q_t} = \frac{1}{k_2 q_e^2} + \frac{t}{q_e} \quad (4)$$

where  $k_2$  is the steady-state velocity constant of second-order adsorption (g mg<sup>-1</sup> min<sup>-1</sup>).

## Results and discussion

### Characterization

Figure 1 displays the XRD traces of  $\text{Fe}_3\text{O}_4$ , GO, BT, MrGO and MrGO-BT. The basal reflections of  $\text{Fe}_3\text{O}_4$  at  $d_{220}$ ,  $d_{311}$ ,  $d_{400}$ ,  $d_{422}$ ,  $d_{511}$  and  $d_{440}$  were 2.96, 2.52, 2.09, 1.71, 1.61 and 1.48 Å, respectively (Fig. 1a,d,e). The positions of the  $\text{Fe}_3\text{O}_4$  peaks remained unaltered (Fig. 1d,e), demonstrating that MrGO and MrGO-BT still had a solid  $\text{Fe}_3\text{O}_4$  crystal structure. A peak (4.67 Å) for rGO occurred in the XRD traces for MrGO and MrGO-BT (Fig. 1d,e; Zhang *et al.*, 2018), revealing that GO was reduced to rGO, but the  $d_{001}$  peak of GO (7.38 Å) disappeared, as can be seen in Fig. 1b. The primary  $d_{001}$  peak of BT occurred at 13.33 Å (Fig. 1c), which moved to 15.21 Å with the introduction of CS into BT (Fig. 1e). This might be because CS was introduced into the BT interlayer, increasing the basal space of BT (Liu *et al.*, 2018; Jimtaisong & Sarakonsri, 2019), which would increase the capacity of the substance to bind heavy-metal ions.

The FTIR spectra of BT, GO,  $\text{Fe}_3\text{O}_4$ , CS, MrGO and MrGO-BT are shown in Fig. 2. The absorptions at 1643 and 3420  $\text{cm}^{-1}$  were caused by the twisting and flexion vibrations of the hydroxyl group in BT, respectively (Fig. 2a; Perelomov *et al.*, 2016). BT showed a signal at 1038  $\text{cm}^{-1}$  for the Si–O group (Liu *et al.*, 2011), and two adsorption peaks at 521 and 467  $\text{cm}^{-1}$  were caused by the bending vibrations of Si–O–Si and Al–O–Si of BT, respectively (Yang *et al.*, 2010). The aluminium hydroxyl group on the smectite was found to vibrate strongly and was responsible for the peak value at 3635  $\text{cm}^{-1}$ . The hydroxyl group in GO and adsorbed water were responsible for the peaks between 3000 and 3600  $\text{cm}^{-1}$  (Fig. 2b; Liu *et al.*, 2019), and the peak at 1730  $\text{cm}^{-1}$  demonstrated the C=C bending of the  $\text{sp}^2$  carbon and the flexion vibrato of water (Kong *et al.*, 2019; Wang *et al.*, 2020). A distinct Fe–O peak could be seen at 580  $\text{cm}^{-1}$  (Fig. 2c). The C=O twisting vibration of -NHCO- and the N–H bending vibration of -NH<sub>2</sub> were attributable to the distinct bands at 1662 and 1596  $\text{cm}^{-1}$  (Jiang *et al.*, 2020).

The functional organization of rGO,  $\text{Fe}_3\text{O}_4$  and CS was seen in the FTIR spectrum of MrGO (Fig. 2e). The signal at 1730  $\text{cm}^{-1}$  disappeared, confirming that the carboxyl group on GO could be reduced completely. It is possible that the disappearance of

the C=O asymmetric stretching vibration at 1662  $\text{cm}^{-1}$  was caused by the connection between CS and oxygen-containing groups of rGO, as well as electrostatic forces attracting CS to the negatively charged organic compounds of rGO (Zhou *et al.*, 2016; Qi *et al.*, 2018). The peaks between 3300 and 3600  $\text{cm}^{-1}$  in MrGO were attributed to rGO, but the intensity was weaker than that seen for GO, demonstrating that GO had not been reduced completely and that the surface of rGO still contained abundant hydroxyl groups. The interaction between the nitrogen-containing groups of CS and the hydroxyl bond of rGO may have been responsible for the red shift of N–H from 1596 to 1552  $\text{cm}^{-1}$ . MrGO showed a blue shift of the characteristic Fe–O peak from 580 to 620  $\text{cm}^{-1}$ , which was due to the local electron rearrangement on the nanoparticle surface (Yang *et al.*, 2018).

The structural bonds of BT and MrGO were observable in the FTIR spectra of MrGO-BT (Fig. 2f), but the vibration peak at 3635  $\text{cm}^{-1}$  disappeared. This is believed to be the consequence of the condensation of the surface functional groups of BT with the hydroxyl groups of rGO and CS. Following the addition of BT, a decrease in the N–H ratio and an increase in the -OH ratio led to a reduction in the peak at 1552  $\text{cm}^{-1}$  and an increase in the peaks at in 3300 and 3600  $\text{cm}^{-1}$ . The decrease in peak area at 1038  $\text{cm}^{-1}$  was attributed to a reduction in the overall proportion of BT in MrGO-BT.

The TEM images of MrGO and MrGO-BT are shown in Fig. 3. The TEM images of MrGO (Fig. 3a,b) illustrate the presence of  $\text{Fe}_3\text{O}_4$ , CS and rGO sheets in the MrGO composite.  $\text{Fe}_3\text{O}_4$  coated with CS formed a 200 nm sphere, and the CS was loose and flocculent (Liu *et al.*, 2016). The rGO sheets had sandwiched the CS and  $\text{Fe}_3\text{O}_4$  (Fig. 3b), indicating that rGO and CS acted as a wall, protecting  $\text{Fe}_3\text{O}_4$  from acid corrosion. The TEM image of BT (Fig. S1) demonstrates that BT presented a lamellar stacking structure, with dense lamellae in the centre. The image of MrGO-BT (Fig. 3c) shows that MrGO was located above BT, but the section of BT that was not covered by MrGO exhibited the characteristic layered structure and stacking features (Zhang *et al.*, 2015).

The EDS mapping of MrGO-BT is depicted in Fig. 4. Because of its layered structure, the distribution of the elements Fe, Si, Al, C, O and N was not uniform. A sandwich structure with rGO as

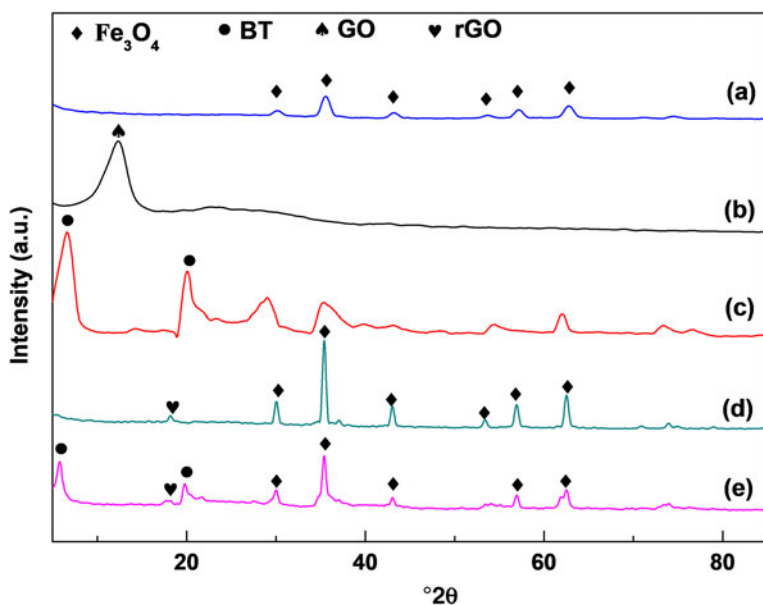
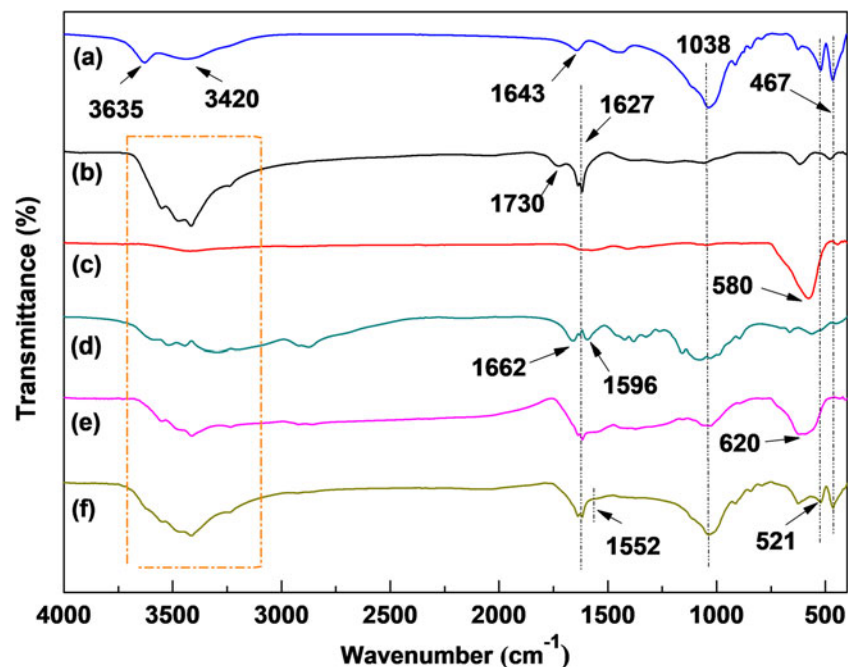


Fig. 1. XRD traces of (a)  $\text{Fe}_3\text{O}_4$ , (b) GO, (c) BT, (d) MrGO and (e) MrGO-BT.



**Fig. 2.** FTIR spectra of (a) BT, (b) GO, (c)  $\text{Fe}_3\text{O}_4$ , (d) CS, (e) MrGO and (f) MrGO-BT.

the sandwich layer,  $\text{Fe}_3\text{O}_4$  as the core and CS/BT as the shell was the proposed structural hypothesis based on the fact that the Fe was surrounded by a significant amount of C and O and that some Si and Al were spread over MrGO-BT.

Figure 5 shows the  $\text{N}_2$ -sorption isotherm of MrGO-BT. In accordance with the International Union of Pure and Applied Chemistry (IUPAC) classification, MrGO-BT showed a class IV isotherm and is a mesoporous adsorption material. The presence of the H3-type hysteresis ring in the  $P/P_0$  range of 0.4–1.0 indicated the presence of slits created by the accumulation of flake particles in MrGO-BT. According to the pore-structure results obtained (Table 1), MrGO-BT had a specific surface area of  $95.46 \text{ m}^2 \text{ g}^{-1}$ , a pore volume of  $0.143 \text{ m}^3 \text{ g}^{-1}$  and a mean pore size of 7.03 nm. The elimination of Cr(VI) was improved at greater pore volumes and specific surface areas, which facilitated ion exchange.

Figure 6 illustrates the MrGO-BT surface  $\zeta$ -potential fluctuations between pH 1.0 and 9.0. It can be seen that the pH at the point of zero charge ( $\text{pH}_{\text{pzc}}$ ) of MrGO-BT was close to 3.1. As

the pH increased, the  $\zeta$ -potential decreased steadily. When pH was  $<3.1$ , the surface of MrGO-BT was positively charged due to its  $\text{H}^+$  coating, helping it to adsorb and dissociate the oxygenated anions of Cr(VI). By contrast, because MrGO-BT had a negatively charged surface, the oxygenated anions of Cr(VI) led to electrostatic repulsion, decreased its adsorption capacity gradually.

### Cr(VI) elimination with MrGO-BT

#### Processing parameters

Under the conditions of a solution temperature of  $20^\circ\text{C}$ , an initial pH value of 4.6, a reaction time of 40 min and a beginning concentration of  $100 \text{ mg L}^{-1}$ , Cr(VI) elimination with MrGO-BT at doses of  $0.55\text{--}5.00 \text{ g L}^{-1}$  is shown in Fig. S2a. Increasing adsorption ability of Cr(VI) with MrGO-BT was observed with increasing adsorbent dosage, reaching a maximum value ( $22.6 \text{ mg g}^{-1}$ ) at  $\sim 1 \text{ g L}^{-1}$ . A possible explanation for this is that with the increasing dosage of MrGO-BT, the total number of adsorption sites of

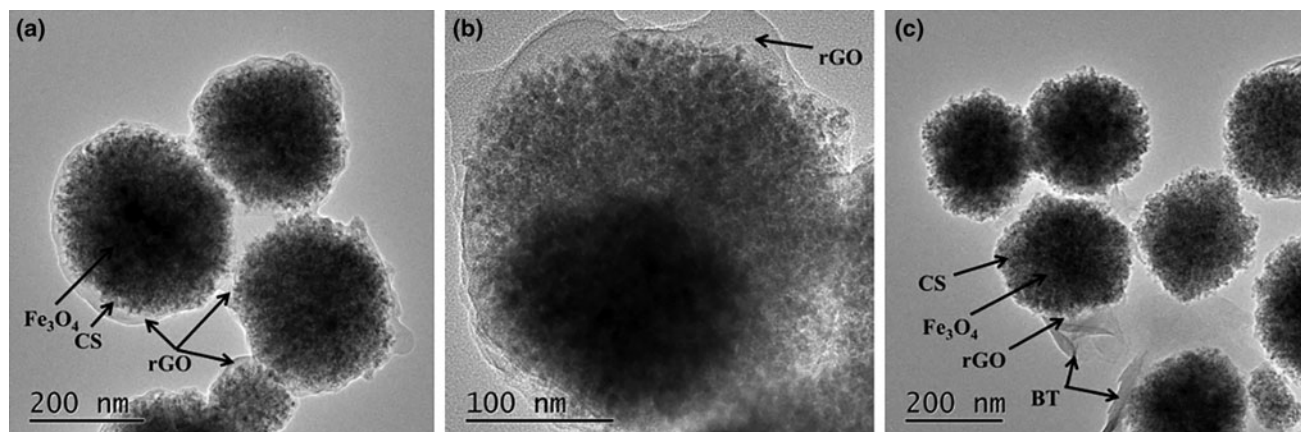


**Fig. 3.** TEM images of (a,b) MrGO and (c) MrGO-BT.

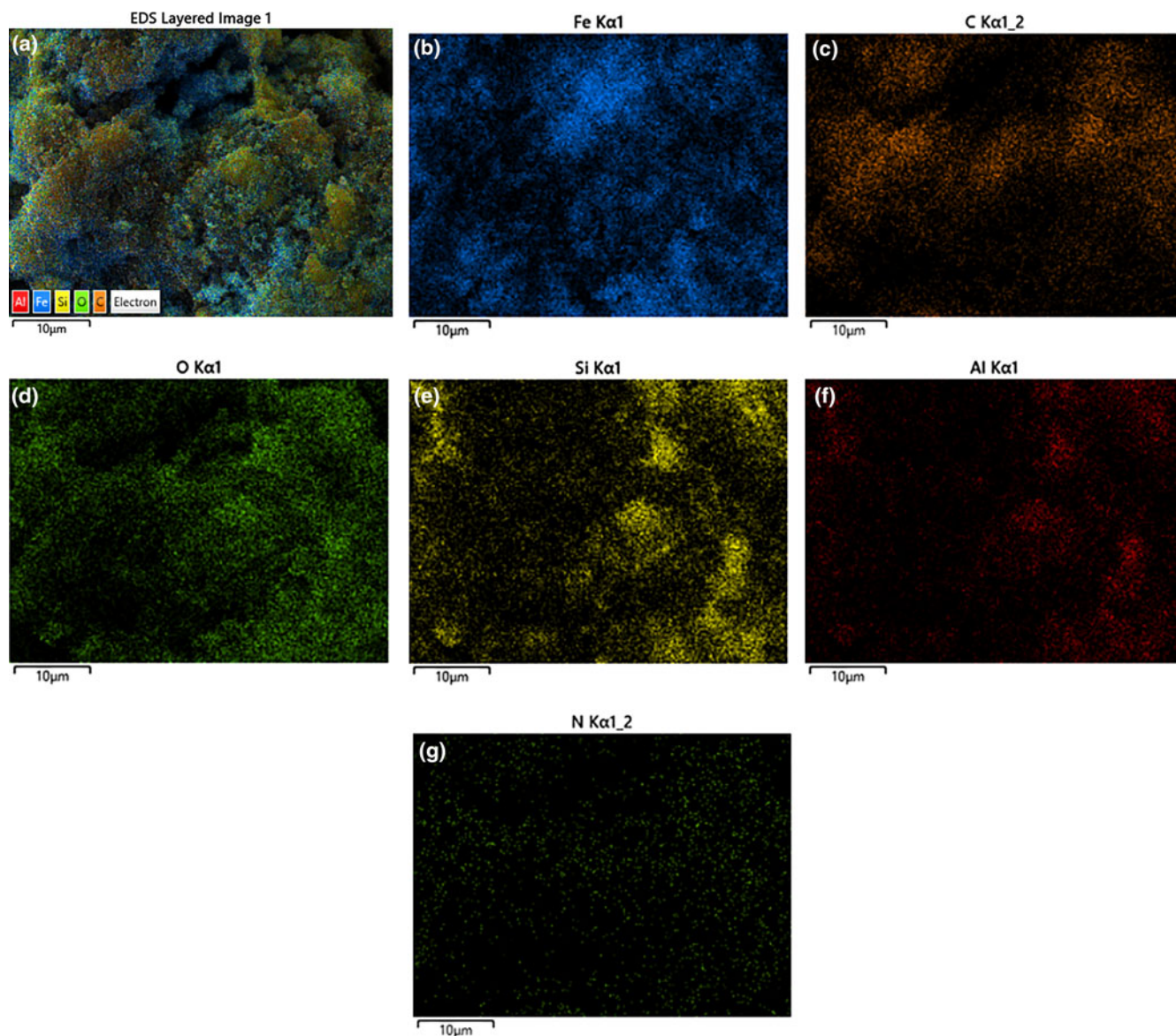


Fig. 4. EDS mapping images of MrGO-BT. (a) Layered EDS image and (b–g) elemental mapping of MrGO-BT.

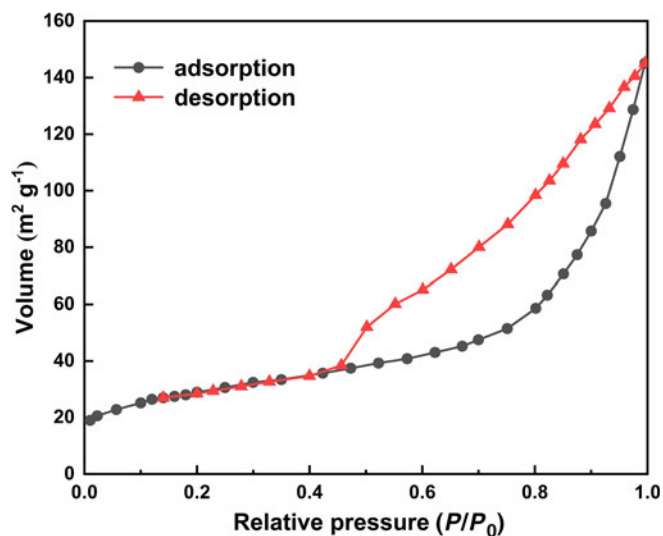


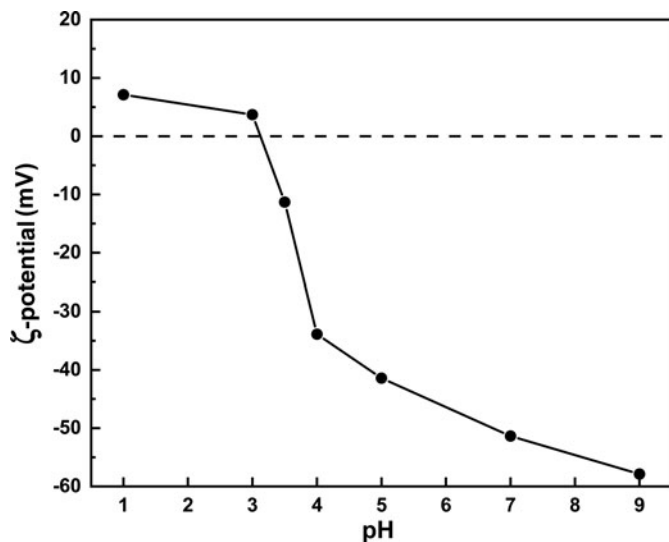
Fig. 5.  $N_2$  adsorption–desorption curve of MrGO-BT.

Cr(VI) increased and so the elimination rate also increased. The ability of MrGO-BT to adsorb Cr(VI) was reduced at doses  $>1 \text{ g L}^{-1}$ . This could be because of the adsorption sites of MrGO-BT being unsaturated and having a greater number of vacant sites at increased dosages (Feng *et al.*, 2019). Therefore, the optimal adsorbent dosage of MrGO-BT was chosen as  $1 \text{ g L}^{-1}$ .

The impact of Cr(VI) was explored at  $20^\circ\text{C}$  and pH 1–9. The adsorption ability of MrGO-BT for Cr(VI) declined as pH increased (Fig. S2b).  $\text{HCrO}_4^-$  and  $\text{Cr}_2\text{O}_7^{2-}$  are present primarily at pH 1–6, but the pH of  $\text{H}_2\text{CrO}_4$  is  $<1$ . At lower pH, there were numerous  $\text{H}^+$  ions, and these induced greater positively charged ions (e.g.  $-\text{NH}_3^+$ ), which favoured the diffusion of the negatively charged chromate ions into the bulk of MrGO-BT due to electrostatic attraction (Niu *et al.*, 2018). This adsorption ability decreased as the pH reduced from 6 to 9 because the significant level of  $\text{OH}^-$  in the solution precluded the diffusion of Cr(VI) (Jin *et al.*, 2014). As a result, pH 1 was chosen the ideal value for MrGO-BT to adsorb Cr(VI).

**Table 1.** Pore structure of MrGO-BT.

Material	Specific surface area (m <sup>2</sup> g <sup>-1</sup> )	Pore volume (cm <sup>3</sup> g <sup>-1</sup> )	Pore size (nm)
MrGO-BT	95.46	0.143	7.03

**Fig. 6.** ζ-potential of MrGO-BT.**Table 2.** Thermodynamic parameters of Cr(VI) removal with MrGO-BT.

R <sup>2</sup>	ΔH <sup>0</sup> (kJ mol <sup>-1</sup> )	ΔS <sup>0</sup> (J (mol K <sup>-1</sup> ) <sup>-1</sup> )	ΔG <sup>0</sup> (kJ mol <sup>-1</sup> )				
			20°C	30°C	40°C	50°C	60°C
0.98	-4.87	-10.02	-1.93	-1.83	-1.73	-1.63	-1.53

The effect on Cr(VI) at the initial concentration range of 20–100 mg L<sup>-1</sup> was explored. Figure S2c shows rapidly increasing adsorption after 40 min, reaching saturation after 150 min. The maximum adsorption ability achieved was 69 mg g<sup>-1</sup> at an initial concentration of Cr(VI) of 100 mg L<sup>-1</sup> and a reaction time of 150 min, and adsorption ability was associated positively with initial Cr(VI) concentration. This indicated that the initial concentration was related to the pressure gradient and that a greater initial concentration of Cr(VI) made it easier for Cr(VI) to move from the solution to the particle surface. However, the greatest elimination rate of 90% was achieved at an initial

**Table 3.** Kinetic models of Cr(VI) adsorption on MrGO-BT.

T (°C)	C <sub>0</sub> (mg L <sup>-1</sup> )	q <sub>e</sub> (mg g <sup>-1</sup> )	Pseudo-first order model			Pseudo-second order model		
			q <sub>1e</sub> (mg g <sup>-1</sup> )	k <sub>1</sub> (min <sup>-1</sup> )	R <sub>1</sub> <sup>2</sup>	q <sub>2e</sub> (mg g <sup>-1</sup> )	k <sub>2</sub> (g mg <sup>-1</sup> min <sup>-1</sup> )	R <sub>2</sub> <sup>2</sup>
20	20	18.0	16.1	0.142	0.90	17.7	0.0118	0.96
	40	33.6	30.2	0.122	0.92	33.0	0.0058	0.98
	60	48.8	43.7	0.124	0.93	47.8	0.0040	0.98
	80	61.2	56.3	0.0674	0.94	63.0	0.0015	0.98
	100	69.0	62.7	0.0684	0.93	70.0	0.0014	0.97
30	100	67.0	61.9	0.0641	0.93	69.3	0.0013	0.98
40	100	66.3	61.0	0.0620	0.92	68.4	0.0013	0.97

concentration of 20 mg L<sup>-1</sup>, and the elimination rate was correlated inversely with the initial concentration of Cr(VI). Therefore, the initial concentration of Cr(VI) was chosen as 20 mg L<sup>-1</sup> and the reaction time was selected to be 150 min.

The temperature-dependent equilibrium constant K<sub>c</sub> (q<sub>e</sub>/q<sub>c</sub>) can be used for the calculation of thermodynamic parameters. Changes in enthalpy (ΔH<sup>0</sup>) and entropy (ΔS<sup>0</sup>) during the adsorption process were calculated using Equation 5:

$$\ln K_c = \frac{\Delta S^0}{R} - \frac{\Delta H^0}{RT} \quad (5)$$

where R is the perfect gas constant and T (K) is the temperature. ΔG<sup>0</sup> is the Gibbs free energy from a specific adsorption, which can be determined using Equation 6:

$$\Delta G^0 = \Delta H^0 - T\Delta S^0 \quad (6)$$

The experimental results are fitted to obtain the values of ΔG<sup>0</sup>, ΔH<sup>0</sup> and ΔS<sup>0</sup> for Cr(VI) adsorption.

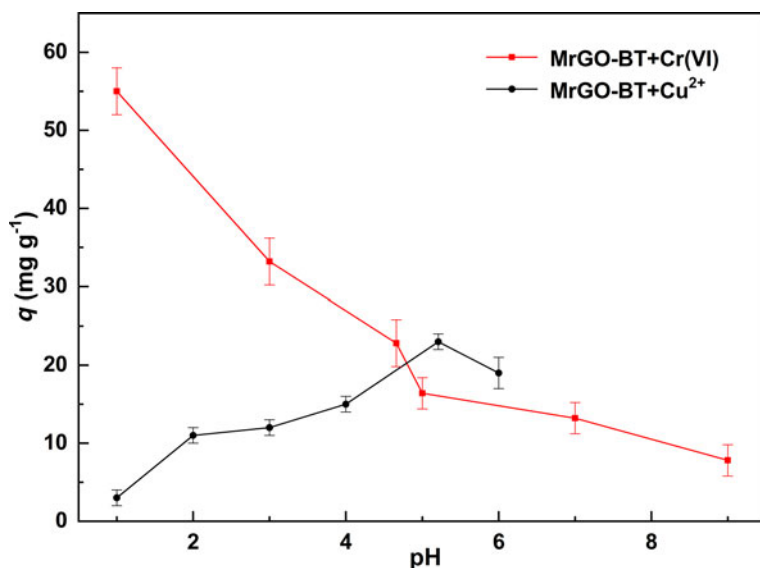
The experiments regarding the adsorption isotherm were undertaken by dissolving 100 mg MrGO-BT in a beaker containing 100 mL of a temperature-varying Cr(VI) solution at pH 1 under continuous mechanical agitation. The values of ΔH<sup>0</sup> and ΔS<sup>0</sup> derived from the fitted equation were -4.87 kJ mol<sup>-1</sup> and -10.02 J (mol K<sup>-1</sup>)<sup>-1</sup> (Table 2), demonstrating that Cr(VI) elimination with MrGO-BT is an exothermic process and increases in randomness. The ΔG<sup>0</sup> values at 20°C, 30°C, 40°C, 50°C and 60°C were -1.93, -1.83, -1.73, -1.63 and -1.53 kJ mol<sup>-1</sup>, respectively (Table 2), indicating that Cr(VI) was adsorbed spontaneously on MrGO-BT. As the temperature increased, the amount of Cr(VI) eliminated with MrGO-BT decreased slightly (Fig. S2d), indicating that Cr(VI) was adsorbed preferentially at lower temperatures.

#### Adsorption kinetics study

The adsorption kinetics of Cr(VI) were explored at an initial pH of 1. Pseudo-first order and pseudo-second order models might represent Cr(VI) elimination on MrGO-BT accurately (Fig. S3), as the correlation coefficient (R<sup>2</sup>) resulting from the linear regression ranged from 0.90 to 0.99 (Table 3). The findings show that physicochemical adsorption may be used to control Cr(VI) elimination with MrGO-BT (Liu *et al.*, 2020; Zhong *et al.*, 2020; Zhu *et al.*, 2020). The q<sub>e</sub> value of the pseudo-second order kinetic model was more similar to the observational data than that of the pseudo-first order model and the R<sup>2</sup> value was greater. This indicates that the pseudo-second order kinetic model was a superior fit in terms of the adsorption of Cr(VI) with MrGO-BT. As the sorbent and adsorbate contribute or transfer

**Table 4.** Isotherm parameters for Cr(VI) adsorption.

Langmuir model			Freundlich model			
$q_{\max}$ (mg g <sup>-1</sup> )	$K_L$ (L mg <sup>-1</sup> )	$R^2$	$q_{\max}$ (mg g <sup>-1</sup> )	$K_F$ ((mg g <sup>-1</sup> )(L mg <sup>-1</sup> ) <sup>1/n</sup> )	$n$	$R^2$
91.5	0.10	0.98	123.3	15.2	2.2	0.96

**Fig. 7.** Adsorption on Cu<sup>2+</sup> and Cr(VI) at various pH values. Reaction conditions: reaction time = 40 min, dosage = 1 g L<sup>-1</sup>, initial concentration = 100 mg L<sup>-1</sup>, temperature = 20°C.**Table 5.** Comparison of various adsorbents for Cr(VI) adsorption.

Adsorbents	pH and temperature	Adsorption capacity (mg g <sup>-1</sup> )	References
MrGO-BT	pH = 1.0 T = 20°C	91.50	This work
GCM (reduced graphene oxide-montmorillonite)	pH = 2.0 T = 20°C	12.86	Zhang <i>et al.</i> (2015)
α-FeOOH/CMSs	pH = 3.0 T = 25°C	29.37	Zhang <i>et al.</i> (2019)
HMK	pH = 5.5 T = 30°C	27.80	Jin <i>et al.</i> (2014)
Magnetic biochar	pH = 1.0 T = 30°C	27.20	Shi <i>et al.</i> (2018)
AS-GO	pH = 2.0 T = 55°C	215.20	He <i>et al.</i> (2017)

AS = 3-aminopropyltriethoxysilane; CMS = carbon microsphere; HMK = hexadecyltrimethylammonium chloride-modified kaolinite.

electrons during chemical sorption, chemisorption may be the rate-limiting step.

During continued mechanical shaking, 100 mg MrGO-BT was added to a beaker containing 100 mL Cr(VI) solution with variable starting concentrations and pH values to test the adsorption isotherm. The Cr(VI) adsorption on MrGO-BT was agitated for 150 min at 20°C. The Freundlich and Langmuir isothermal models in Table 4 & Fig. S4 illustrate the greatest adsorption of Cr(VI) at 20°C, with values of 91.5 and 123.3 mg g<sup>-1</sup>, respectively. The Freundlich isothermal model had a lower  $R^2$  than that of the Langmuir isothermal model. The Langmuir isothermal model is preferred for Cr(VI) adsorption with MrGO-BT based on the

**Table 6.** Influence of Cu<sup>2+</sup> on Cr(VI) adsorption. Reaction conditions: reaction time = 150 min, dosage = 1 g L<sup>-1</sup>, starting concentration = 20 mg L<sup>-1</sup>, temperature = 20°C, pH = 1.0.

Solution	Ion	Initial concentration (mg L <sup>-1</sup> )	Equilibrium concentration (mg L <sup>-1</sup> )	Removal rate (%)
Cu <sup>2+</sup>	Cu <sup>2+</sup>	20.00	12.00	40.00
Cr(VI)	Cr(VI)		10.66	46.74
Cu <sup>2+</sup> and Cr(VI)	Cu <sup>2+</sup>		13.34	33.33
	Cr(VI)		9.53	52.36

parameters in Table 4. In Table 5, the Cr(VI) elimination abilities with MrGO-BT and data from previous reports are contrasted.

#### Effect of Cu<sup>2+</sup> on Cr(VI) adsorption

Cu<sup>2+</sup> was chosen as the coexisting ion due to Cr-contaminated water containing a variety of cations. As illustrated in Fig. 7, the pH ranged from 1.0 to 5.2 initially with only Cu<sup>2+</sup> in solution. As the pH of the solution increased, Cu<sup>2+</sup> adsorption ability increased as H<sup>+</sup> and Cu<sup>2+</sup> engaged in stronger competition for the active sites. However, when the pH increased beyond 5.2, Cu<sup>2+</sup> started to precipitate as Cu(OH)<sub>2</sub>, which reduced the amount of Cu<sup>2+</sup> (Qin *et al.*, 2019; Wu *et al.*, 2019). Ultimately, both of these outcomes reflect an increase in saturation. In addition, adsorption experiments were conducted on the mixture of Cu<sup>2+</sup> and Cr(VI). Table 6 compares the Cu<sup>2+</sup> and Cr(VI) adsorption results and shows that Cu<sup>2+</sup> removal in the mixed-ion adsorption process was reduced from 40.00% to 33.33%; however, the elimination rate of Cr(VI) increased from 46.74% to 52.36%.

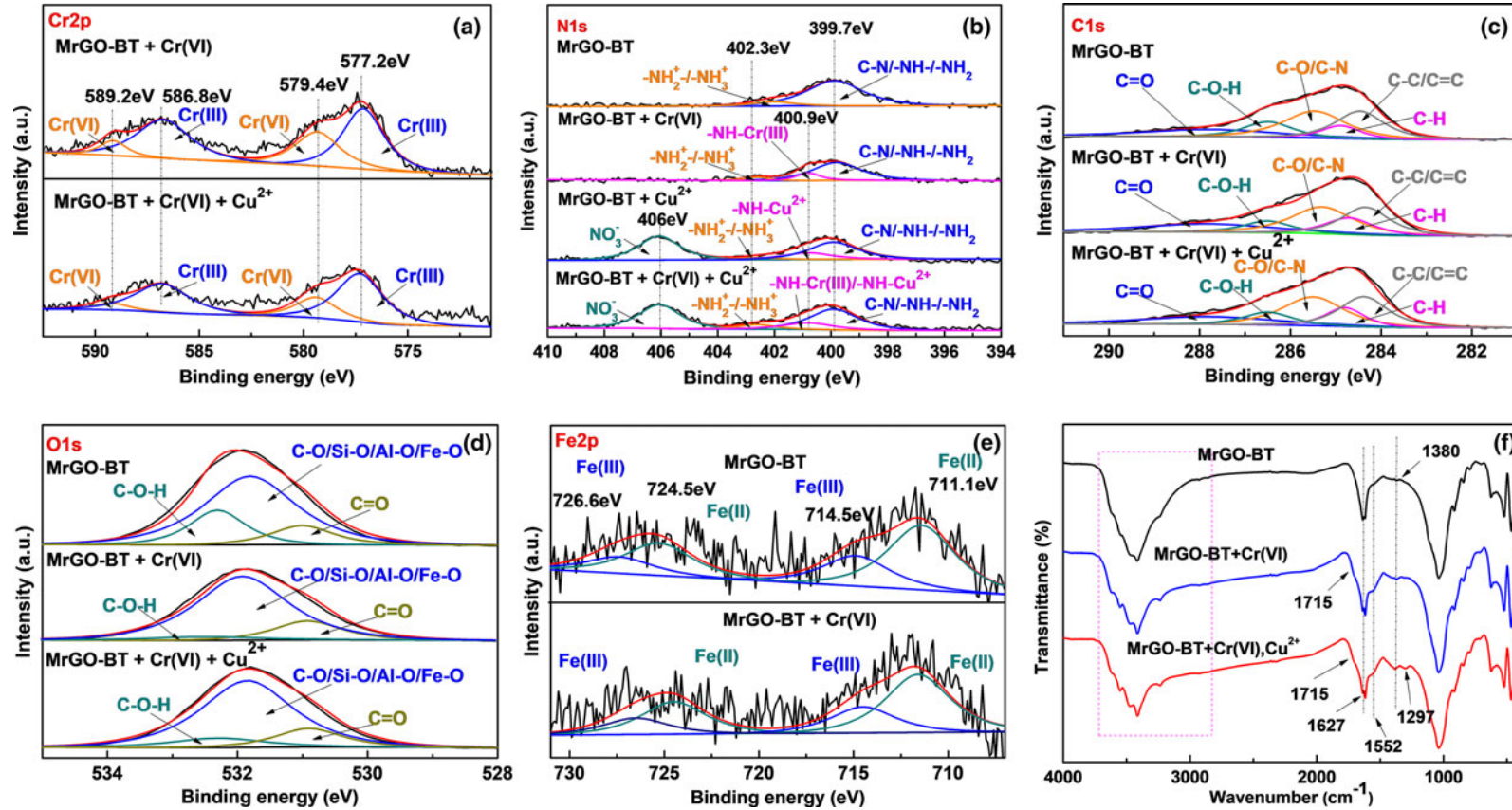


Fig. 8. (a–e) XPS and (f) FTIR spectra of MrGO-BT before and after adsorption.



This implies that Cr(VI) and Cu<sup>2+</sup> might compete for the same adsorption sites. However, other mechanisms were also identified in this study. This competition resulted from the increased cation strength of the mixed-ion solution after the addition of Cu<sup>2+</sup> (Zhao *et al.*, 2019). Alternatively, MrGO-BT favoured positively charged Cu<sup>2+</sup> in the mixture of the Cu<sup>2+</sup> and Cr(VI) system, which neutralized parts of the negative charge on the surface of MrGO-BT and increased the electrostatic attraction of HCrO<sub>4</sub><sup>-</sup> and Cr<sub>2</sub>O<sub>7</sub><sup>2-</sup> (the main forms of chromate at pH 4.8), improving Cr(VI) elimination (Tanboonchuy *et al.*, 2012; Lv *et al.*, 2013).

### Mechanism analysis

The elemental composition before and after Cr(VI) removal with MrGO-BT was analysed using XPS. Figure 8a shows component curves used to fit the Cr2p peak, and the binding energies were 577.2, 579.4, 586.8 and 589.2 eV. The binding energies at 577.2 and 579.4 eV are associated with Cr2p<sub>3/2</sub> orbitals, whereas the peaks at 586.8 and 589.2 eV are identified with Cr2p<sub>1/2</sub> orbitals. Cr(III) may be inferred from the bonding energies of 577.2 and 586.8 eV, whereas the peaks at 579.4 and 589.2 eV may be considered as evidence of Cr(VI) (Ma *et al.*, 2012). The results indicate that the MrGO-BT included Cr(VI) and Cr(III) and that Cr(VI) was transformed, to a significant extent, to Cr(III). According to the fitting results and peaks pattern, Cr(VI) accounted for 27.5% of the total Cr in MrGO-BT after adsorbing Cr(VI) and Cr(VI) made up 38.0% following the adsorption of the mixed ions.

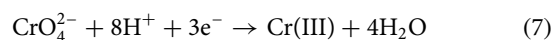
To investigate this phenomenon further, the O, N and C of MrGO-BT were analysed using XPS. Figure 8b shows that N after Cr(VI) adsorption was present in the forms of -NH<sub>2</sub> (399.7 eV), -NH-Cr(III) (400.9 eV) and C-N/-NH<sub>2</sub><sup>+</sup>/NH<sub>3</sub><sup>+</sup> (402.3 eV) species (Zhu *et al.*, 2016; Ghanbari & Nejabati, 2020). After the mixed ions were adsorbed, NO<sub>3</sub><sup>-</sup> (406 eV) was found in MrGO-BT after the reaction of the mixed-ion solution (Fig. 8b), showing similar XPS results to MrGO-BT after Cu<sup>2+</sup> adsorption alone, with equal intensities for the two NO<sub>3</sub><sup>-</sup> peaks. Moreover, the two peak intensities were equal, proving that NO<sub>3</sub><sup>-</sup> originated from the Cu(NO<sub>3</sub>)<sub>2</sub> solution. Therefore, it was concluded that the presence elemental N and N-containing groups was unrelated to the decline in Cr(VI).

The peak fitting in Fig. 8c,d shows several interesting phenomena. Figure 8c shows the splitting peaks of C1s for C-C/C=C (284.4 eV), C-O/C-N (285.5 eV), C-O-H (286.5 eV), C-H (284.8 eV) and C=O (287.9 eV) (Mei *et al.*, 2020). For clarity, fresh MrGO-BT, MrGO-BT after Cr(VI) adsorption and MrGO-BT after adsorption of the mixed ions are labelled as A, B and C, respectively. The C-H and C=O peak areas were in the order of B > C > A, and the C-O-H peak area was in the order of A > C > B, while the C-C, C=C, C-O and C-N peak areas remained unchanged across A, B and C. These findings reveal that Cr(VI) could react with C-O-H to form H-C=O, and Cu<sup>2+</sup> could hinder the decrease in Cr(VI) because of the surface complexation and chelation between Cu<sup>2+</sup> and C-O-H or -NH<sub>2</sub>. Figure 8d depicts the splitting peaks of O1s for C=O (530.9 eV), Si-O/C-O/Al-O/Fe-O (531.8 eV) and C-O-H (532.3 eV) (Zhang *et al.*, 2020). The C=O peak areas are displayed the order of B > C > A and the C-O-H peak area showed the order of A > C > B, while the Si-O/C-O/Al-O/Fe-O peak areas remained unaltered across A, B and C. These variations corroborated the conclusions derived from Fig. 8c. Figure 8e shows XPS peaks at 711.1 and 724.5 eV for Fe(II) and 714.5 and 726.6 eV for Fe(III) (Dong *et al.*, 2020). After eliminating Cr(VI) and the

coexisting ions, the peak area remained unaltered, indicating that Fe(II) had no impact on the Cr(VI) reduction reaction. The high-resolution XPS spectrum of Cu2p for MrGO-BT after mixed-ion adsorption showed bands of Cu2p<sub>1/2</sub> and Cu2p<sub>3/2</sub> at 953.3 and 933.5 eV, respectively (Fig. S5). The former was assigned to free Cu<sup>2+</sup>, while the latter was assigned to Cu<sup>2+</sup> that chelated with amino groups on MrGO-BT (Li *et al.*, 2019).

Figure 8f shows the FTIR spectra of MrGO-BT before and after adsorbing heavy-metal ions. The bands ranging from 3000 to 3600 cm<sup>-1</sup> decreased after Cr(VI) elimination due to the oxidation of C-O-H to H-C=O, whereas the band at 1715 cm<sup>-1</sup> appeared as a result of the production of H-C=O on MrGO-BT. The peak area increased at 1552 cm<sup>-1</sup>, indicating the appearance of NH<sub>3</sub><sup>+</sup> in the acidic solution. These results are consistent with the XPS analysis and indicate that C-O-H supplied electrons for the reduction of Cr(VI) and was oxidized to H-C=O. The bands at 1380 and 1297 cm<sup>-1</sup> could be generated *via* amino group chelation with Cr(III) and Cu<sup>2+</sup>, respectively.

Generally, the single metal ion (Cr(VI)) adsorption mechanism by MrGO-BT proceeded as follows: portions of the Cr(VI) reacted with C-O-H on MrGO-BT to generate H-C=O and Cr(III) as shown in Equations 7 and 8:



The electrons required for Cr(VI) reduction in mixed-metal ion adsorption (Cr(VI) and Cu<sup>2+</sup>) were supplied by C-O-H on MrGO-BT. The p*H*<sub>pzc</sub> of MrGO-BT was ~3.1, and at pH values between 1.0 and 3.1 the MrGO-BT adsorbent surface became positively charged *via* strong protonation (-NH<sub>2</sub><sup>+</sup>/NH<sub>3</sub><sup>+</sup>), increasing electron attraction *via* electrostatic forces and also increasing the elimination rate of Cr(VI). In the presence of Cu<sup>2+</sup> (pH 4.8), Cu<sup>2+</sup> was adsorbed preferentially on MrGO-BT because of

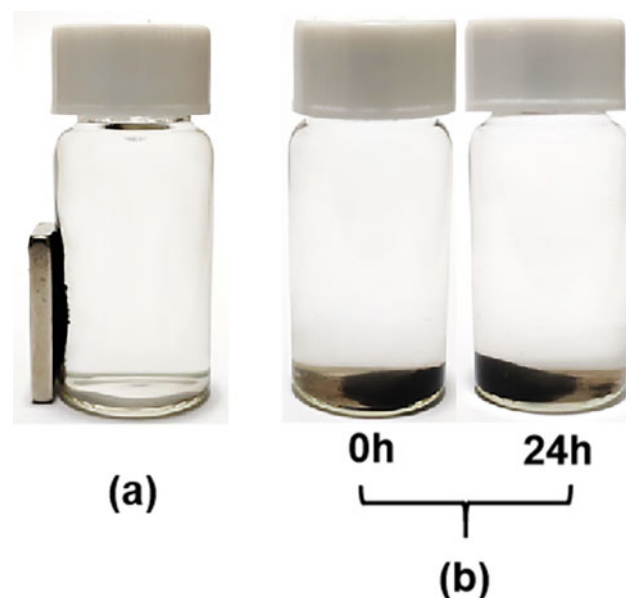


Fig. 9. (a) MrGO-BT magnetic recovery experiment. (b) MrGO-BT immersed in water for 0 or 24 h at pH 1.

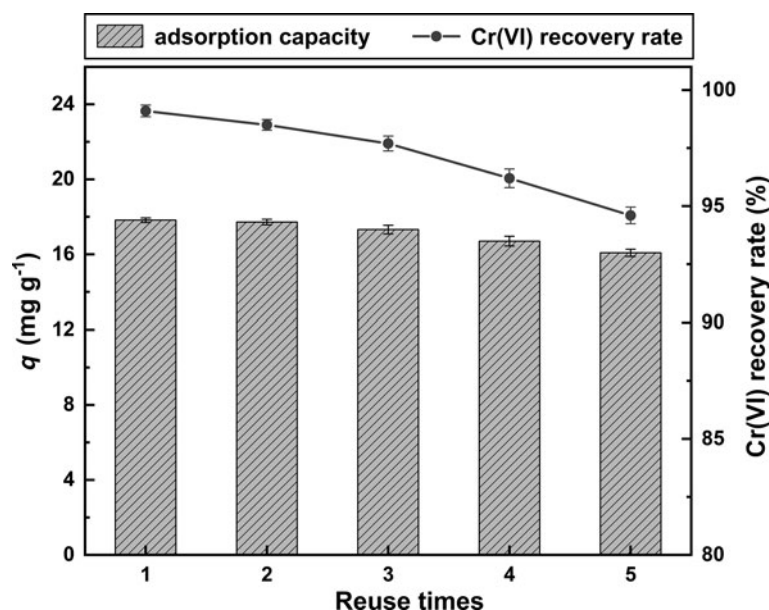


Fig. 10. Recycling performance of MrGO-BT.

electrostatic attraction, neutralizing part of the negative charge, thereby reducing the electrostatic repulsion of negatively charged Cr(VI) and increasing the elimination rate of Cr(VI). In addition, there might have been exchange of cations between  $\text{Cu}^{2+}$  and Cr(III) and the BT interlayer, as well as chelation with  $-\text{NH}_2$  on MrGO-BT to form  $-\text{NH}-\text{Cr}(\text{III})$  or  $-\text{NH}-\text{Cu}^{2+}$ . MrGO-BT removed most of the Cr(VI) *via* electrostatic adsorption, the redox reaction and chelation.

#### Magnetic response, acid resistance and reusability of MrGO-BT

The magnetic response of MrGO-BT was tested by submerging the sample in a water solution. Then MrGO-BT was attracted to a magnet. As is shown in Fig. 9a, the MrGO-BT in the solution was attracted to the magnetic side. To evaluate the acid resistance of MrGO-BT, the sample was immersed in acidic water (pH 1.0) for 24 h (Fig. 9b). MrGO-BT showed strong acid resistance, as inductively coupled plasma-optical emission spectroscopy indicated the  $\text{Fe}^{3+}$  dissolution mass in the solution to be  $8.59 \mu\text{g}$  and the  $\text{Fe}^{3+}$  dissolution rate to be 0.21%. This corroborates the TEM and FTIR results, which indicated that rGO and CS could shield  $\text{Fe}_3\text{O}_4$  from acid corrosion.

Five repeated sorption processes were performed to evaluate the reusability of MrGO-BT under optimal conditions (Fig. 10). It was observed that the adsorption ability for Cr(VI) by MrGO-BT decreased slightly over repeated sorption processes. This might be because the Cr(VI) adsorbed on MrGO-BT was only desorbed partially in saturated EDTA-2Na solution, with some adsorption sites remaining occupied. The recovery rate of Cr(VI) was 95.6–99.1% after five cycles and the adsorption capacity decreased to  $16.08 \text{ mg g}^{-1}$ , which was only  $1.92 \text{ mg g}^{-1}$  less than that of fresh adsorbent. Therefore, MrGO-BT has good adsorption stability, as demonstrated by the recovery test.

#### Conclusion

MrGO-BT was prepared efficiently and utilized to remove Cr(VI), and it was discovered that MrGO-BT has a stable structure because of the condensation of organic compounds on BT and the  $-\text{OH}$  of rGO and CS. The optimal reaction conditions for

Cr(VI) removal by MrGO-BT were determined to be  $1 \text{ g L}^{-1}$  of adsorbent, pH 1, 150 min of contact time, temperature of  $20^\circ\text{C}$  and an initial Cr(VI) concentration of  $20 \text{ mg L}^{-1}$ . A total of 90% of the Cr(VI) can be removed under these circumstances. The pseudo-second order reaction kinetics and the Langmuir adsorption equation were employed to describe the sorption behaviour of Cr(VI) on MrGO-BT. The greatest adsorption ability for Cr(VI) was  $91.5 \text{ mg g}^{-1}$  at  $20^\circ\text{C}$ . The FTIR spectroscopy and XPS results indicated that Cr(VI) was eliminated by MrGO-BT *via* reduction and adsorption reactions. In an acidic environment,  $-\text{NH}/-\text{NH}_2$  on the surface of MrGO-BT could react with  $\text{H}^+$  to form  $-\text{NH}_2^+/-\text{NH}_3^+$  in solution, which improved the electrostatic attraction to Cr(VI).  $\text{C}-\text{O}-\text{H}$  on MrGO-BT led to the electrostatic attraction of Cr(VI), and  $\text{H}-\text{C}=\text{O}$  and Cr(III) were generated *via* reduction reactions. In addition, the adsorption ability of MrGO-BT for Cr(VI) was increased *via* the addition of  $\text{Cu}^{2+}$  due to electrostatic attraction. MrGO-BT exhibited strong acid resistance and good magnetic responsiveness. It maintained great adsorption ability after five sorption and desorption tests ( $16.08 \text{ mg g}^{-1}$ ). Therefore, Cr(VI) elimination on MrGO-BT holds significant promise for environmental remediation.

**Financial support.** The project is supported by the National Key Basic Research Program of China (No. 2019YFC0408604-4), the Natural Science Foundation of Shanxi Province (201901D111110), the Shanxi Program on Key Research Project (Social Development, 201903D321053), the Shanxi Scholarship Council of China (No. HGKY2019017) and the Shanxi Provincial Foundation for Leaders of Disciplines in Science, China.

**Conflicts of interest.** None.

#### References

- Abu-Nada A., McKay G. & Abdala A. (2020) Recent advances in applications of hybrid graphene materials for metals removal from wastewater. *Nanomaterials*, **10**, 595.
- Almeida J.C., Cardoso C.E.D., Tavares D.S., Freitas R., Trindade T., Vale C. et al. (2019) Chromium removal from contaminated waters using nanomaterials – a review. *TrAC - Trends in Analytical Chemistry*, **118**, 277–291.
- Chen J.D., Liang Q.W., Ploychompoo S. & Luo H.J. (2020) Functional rGO aerogel as a potential adsorbent for removing hazardous hexavalent

- chromium: adsorption performance and mechanism. *Environmental Science and Pollution Research*, **27**, 10715–10728.
- Dong S., Chen Y.X. & Hong C.Q. (2020) Synergetic impedance matching and loss ability towards efficient microwave absorption of Fe<sub>3</sub>O<sub>4</sub> nanoparticles anchored on SiC whiskers via a simple solvothermal method. *Journal of Alloys and Compounds*, **838**, 155558.
- Feng G.R., Ma J.C., Zhang X.P., Zhang Q.F., Xiao Y.Q., Ma Q.L. *et al.* (2019) Magnetic natural composite Fe<sub>3</sub>O<sub>4</sub>-chitosan@bentonite for removal of heavy metals from acid mine drainage. *Journal of Colloid and Interface Science*, **538**, 132–141.
- Ghanbari K. & Nejabati F. (2020) Ternary nanocomposite-based reduced graphene oxide/chitosan/Cr<sub>2</sub>O<sub>3</sub> for the simultaneous determination of dopamine, uric acid, xanthine, and hypoxanthine in fish meat. *Analytical Methods*, **12**, 1650–1661.
- He C., Yang Z.Q., Ding J., Chen Y.C., Tong X.W. & Li Y. (2017) Effective removal of Cr(VI) from aqueous solution by 3-aminopropyltriethoxysilane-functionalized graphene oxide. *Colloids and Surfaces A - Physicochemical and Engineering Aspects*, **520**, 448–458.
- Jiang L., Su C., Wen Y.Y., Zhu Z.J., Liu J., He S.R. *et al.* (2020) Antibacterial activity and long-term stable antibacterial performance of nisin grafted magnetic GO nanohybrids. *Materials Science and Engineering C - Materials for Biological Applications*, **111**, 110809.
- Jimtaisong A. & Sarakonsri T. (2019) Chitosan intercalated bentonite as natural adsorbent matrix for water-soluble sappanwood dye. *International Journal of Biological Macromolecules*, **129**, 737–743.
- Jin X.Y., Jiang M.Q., Du J.H. & Chen Z.L. (2014) Removal of Cr(VI) from aqueous solution by surfactant-modified kaolinite. *Journal of Industrial and Engineering Chemistry*, **20**, 3025–3032.
- Kong Q.P., Wei J.Y., Hu Y. & Wei C.H. (2019) Fabrication of terminal amino hyperbranched polymer modified graphene oxide and its prominent adsorption performance towards Cr(VI). *Journal of Hazardous Materials*, **363**, 161–169.
- Kumar P.A., Ray M. & Chakraborty S. (2007) Hexavalent chromium removal from wastewater using aniline formaldehyde condensate coated silica gel. *Journal of Hazardous Materials*, **143**, 24–32.
- Li L.L., Feng X.Q., Han R.P., Zang S.Q. & Yang G. (2017) Cr(VI) removal via anion exchange on a silver-triazolate MOF. *Journal of Hazardous Materials*, **321**, 622–628.
- Li P.P., Zhang H.L., Xia M.Z., Wang F.Y., Zhu S.D. & Lei W. (2019) The synergistic effect and microscopic mechanism of co-adsorption of three emerging contaminants and copper ion on gemini surfactant modified montmorillonite. *Ecotoxicology and Environmental Safety*, **184**, 109610.
- Liu Z.R., Uddin M.A. & Sun Z.X. (2011) FT-IR and XRD analysis of natural Na-bentonite and Cu(II)-loaded Na-bentonite. *Spectrochimica Acta Part A - Molecular and Biomolecular Spectroscopy*, **79**, 1013–1016.
- Liu J.S., Liu W.X., Wang Y.R., Xu M.J. & Wang B. (2016) A novel reusable nanocomposite adsorbent, xanthated Fe<sub>3</sub>O<sub>4</sub>-chitosan grafted onto graphene oxide, for removing Cu(II) from aqueous solutions. *Applied Surface Science*, **367**, 327–334.
- Liu D.M., Dong C., Zhong J.P., Ren S.L., Chen Y.N. & Qiu T.S. (2020) Facile preparation of chitosan modified magnetic kaolin by one-pot coprecipitation method for efficient removal of methyl orange. *Carbohydrate Polymers*, **245**, 116572.
- Liu Q., Xu M.D., Zhao J., Yang Z., Qi C.Z., Zeng M.F. *et al.* (2018) Microstructure and catalytic performances of chitosan intercalated montmorillonite supported palladium (0) and copper (II) catalysts for Sonogashira reactions. *International Journal of Biological Macromolecules*, **113**, 1308–1315.
- Liu H.H., Hu X.X., Guo H.Q., Zhao J.Y., Li F.R., Zhu D.S. *et al.* (2019) One-step reducing and dispersing graphene oxide via hydroxypropyl hydrazine and its applications in Cu<sup>2+</sup> removal. *Physical Chemistry Chemical Physics*, **21**, 10947–10954.
- Lv X.S., Hu Y.J., Tang J., Sheng T.T., Jiang G.M. & Xu X.H. (2013) Effects of co-existing ions and natural organic matter on removal of chromium (VI) from aqueous solution by nanoscale zero valent iron (nZVI)-Fe<sub>3</sub>O<sub>4</sub> nanocomposites. *Chemical Engineering Journal*, **218**, 55–64.
- Ma H.L., Zhang Y.W., Hu Q.H., Yan D., Yu Z.Z. & Zhai M.L. (2012) Chemical reduction and removal of Cr(VI) from acidic aqueous solution by ethylenediamine-reduced graphene oxide. *Journal of Materials Chemistry*, **22**, 5914–5916.
- Maitlo H.A., Kim K.H., Kumar V., Kim S. & Park J.W. (2019) Nanomaterials-based treatment options for chromium in aqueous environments. *Environment International*, **130**, 104748.
- Marcano D.C., Kosynkin D.V., Berlin J.M., Sinititskii A., Sun Z.Z., Slesarev A.S. *et al.* (2010) Correction to improved synthesis of graphene oxide. *ACS Nano*, **4**, 4806–4814.
- Mei J.F., Zhang H., Mo S.Q., Zhang Y.Z., Li Z.Y. & Ou H.X. (2020) Prominent adsorption of Cr(VI) with graphene oxide aerogel twined with creeper-like polymer based on chitosan oligosaccharide. *Carbohydrate Polymers*, **247**, 116733.
- Muthumareeswaran M.R., Alhoshan M. & Agarwal G.P. (2017) Ultrafiltration membrane for effective removal of chromium ions from potable water. *Scientific Reports*, **7**, 41423.
- Niu J.R., Jia X.X., Zhao Y.Q., Liu Y.F., Zhong W.Z., Zhai Z.L. *et al.* (2018) Adsorbing low concentrations of Cr(VI) onto CeO<sub>2</sub> ZSM-5 and the adsorption kinetics, isotherms and thermodynamics. *Water Science and Technology*, **77**, 2327–2340.
- Peng C.D., He Z.T., Feng J.J., Chen D.M., Ding H., Wang J. *et al.* (2020) Preparation of reduced graphene oxide/montmorillonite composite hydrogel and its applications for chromium(VI) and organic compounds adsorption. *Research on Chemical Intermediates*, **46**, 5345–5359.
- Perelomov L., Sarkar B., Rahman M.M., Goryacheva A. & Naidu R. (2016) Uptake of lead by Na-exchanged and Al-pillared bentonite in the presence of organic acids with different functional groups. *Applied Clay Science*, **119**, 417–423.
- Qi C.Y., Zhao L.Q., Lin Y. & Wu D.Y. (2018) Graphene oxide/chitosan sponge as a novel filtering material for the removal of dye from water. *Journal of Colloid and Interface Science*, **517**, 18–27.
- Qin F.M., Fang Z.Q., Zhou J., Sun C., Chen K.H., Ding Z.X. *et al.* (2019) Efficient removal of Cu<sup>2+</sup> in water by carboxymethylated cellulose nanofibrils: performance and mechanism. *Biomacromolecules*, **20**, 4466–4475.
- Shan D.N., Deng S.B., Jiang C.X., Chen Y., Wang B., Wang Y.J. *et al.* (2018) Hydrophilic and strengthened 3D reduced graphene oxide/nano-Fe<sub>3</sub>O<sub>4</sub> hybrid hydrogel for enhanced adsorption and catalytic oxidation of typical pharmaceuticals. *Environmental Science - Nano*, **5**, 1650–1660.
- Shi S.Q., Yang J.K., Liang S., Li M.Y., Gan Q., Xiao K.K. *et al.* (2018) Enhanced Cr(VI) removal from acidic solutions using biochar modified by Fe<sub>3</sub>O<sub>4</sub>@SiO<sub>2</sub>-NH<sub>2</sub> particles. *Science of the Total Environment*, **628–629**, 499–508.
- Sun Q.L., Sun L., Cai Y.Y., Ye W., Xu S.J., Ji T. *et al.* (2019) Fe<sub>3</sub>O<sub>4</sub>-intercalated reduced graphene oxide nanocomposites with enhanced microwave absorption properties. *Ceramics International*, **45**, 18298–18305.
- Tanboonchuy V., Grisdanurak N. & Liao C.H. (2012) Background species effect on aqueous arsenic removal by nano zero-valent iron using fractional factorial design. *Journal of Hazardous Materials*, **205**, 40–46.
- Tran H.N., Nguyen D.T., Le G.T., Tomul F., Lima E.C., Woo S.H. *et al.* (2019) Adsorption mechanism of hexavalent chromium onto layered double hydroxides-based adsorbents: a systematic in-depth review. *Journal of Hazardous Materials*, **373**, 258–270.
- Wang Z.W., Wang Y.H., Cao S., Liu S.H., Chen Z.M., Chen J.F. *et al.* (2020) Fabrication of core@shell structural Fe-Fe<sub>2</sub>O<sub>3</sub>@PHCP nanochains with high saturation magnetization and abundant amino groups for hexavalent chromium adsorption and reduction. *Journal of Hazardous Materials*, **384**, 121483.
- Wu Z.G., Deng W.J., Zhou W. & Luo J.W. (2019) Novel magnetic polysaccharide/graphene oxide @Fe<sub>3</sub>O<sub>4</sub> gel beads for adsorbing heavy metal ions. *Carbohydrate Polymers*, **216**, 119–128.
- Yang S.T., Zhao D.L., Zhang H., Lu S.S., Chen L. & Yu X.J. (2010) Impact of environmental conditions on the sorption behavior of Pb(II) in Na-bentonite suspensions. *Journal of Hazardous Materials*, **183**, 632–640.
- Yang Z.F., Li L.Y., Hsieh C.T., Juang R.S. & Gandomi Y.A. (2018) Fabrication of magnetic iron oxide@graphene composites for adsorption of copper ions from aqueous solutions. *Materials Chemistry and Physics*, **219**, 30–39.
- Yu Y.J.H., Wang Z., Sun R.J., Chen Z.H., Liu M.C., Zhou X. *et al.* (2021) Self-supported reduced graphene oxide membrane and its Cu<sup>2+</sup> adsorption capability. *Materials*, **14**, 146.

- Zhang Z.L., Luo H.J., Jiang X.L., Jiang Z.J. & Yang C. (2015) Synthesis of reduced graphene oxide–montmorillonite nanocomposite and its application in hexavalent chromium removal from aqueous solutions. *RSC Advances*, **5**, 47408–47417.
- Zhang L., Fu F.L. & Tang B. (2019) Adsorption and redox conversion behaviors of Cr(VI) on goethite/carbon microspheres and akaganeite/carbon microspheres composites. *Chemical Engineering Journal*, **356**, 151–160.
- Zhang H., Xiao R., Li R.H., Ali A., Chen A.L. & Zhang Z.Q. (2020) Enhanced aqueous Cr(VI) removal using chitosan-modified magnetic biochars derived from bamboo residues. *Chemosphere*, **261**, 127694.
- Zhang Y.Y., Yan X.R., Yan Y.Y., Chen D.J., Huang L.H., Zhang J.X. *et al.* (2018) The utilization of a three-dimensional reduced graphene oxide and montmorillonite composite aerogel as a multifunctional agent for wastewater treatment. *RSC Advances*, **8**, 4239–4248.
- Zhao P., Chen S., Zhou J., Zhang S.Y., Huo D.Q. & Hou C.J. (2020) A novel Fe–hemin–metal organic frameworks supported on chitosan-reduced graphene oxide for real-time monitoring of H<sub>2</sub>O<sub>2</sub> released from living cells. *Analytica Chimica Acta*, **1128**, 90–98.
- Zhao L.Q., Chen J.X., Xiong N., Bai Y.T., Yilihamu A., Ma Q. *et al.* (2019) Carboxylation as an effective approach to improve the adsorption performance of graphene materials for Cu<sup>2+</sup> removal. *Science of the Total Environment*, **682**, 591–600.
- Zhong X., Lu Z.P., Liang W. & Hu B.W. (2020) The magnetic covalent organic framework as a platform for high-performance extraction of Cr(VI) and bisphenol a from aqueous solution. *Journal of Hazardous Materials*, **393**, 122353.
- Zhou T.N., Qi X.D., Bai H.W. & Fu Q. (2016) The different effect of reduced graphene oxide and graphene oxide on the performance of chitosan by using homogenous fillers. *RSC Advances*, **6**, 34153–34158.
- Zhu C.Q., Liu F.Q., Zhang Y.H., Wei M.M., Zhang X.P., Ling C. *et al.* (2016) Nitrogen-doped chitosan–Fe(III) composite as a dual-functional material for synergistically enhanced co-removal of Cu(II) and Cr(VI) based on adsorption and redox. *Chemical Engineering Journal*, **306**, 579–587.
- Zhu S.H., Wang S., Yang X., Tufail S., Chen C., Wang X. *et al.* (2020) Green sustainable and highly efficient hematite nanoparticles modified biochar–clay granular composite for Cr(VI) removal and related mechanism. *Journal of Cleaner Production*, **276**, 123009.